Investigation of microstructure evolution during self-annealing in thin Cu films by combining mesoscale level set and ab initio modeling

Hallberg, Håkan; Olsson, Pär

Published in:
Journal of the Mechanics and Physics of Solids

DOI:
10.1016/j.jmps.2016.02.026

2016

Journal of the Mechanics and Physics of Solids 2016, vol. 90, pages 160-178

Investigation of microstructure evolution during self-annealing in thin Cu films by combining mesoscale level set and ab-initio modeling

Håkan Hallberg†, Pär A.T. Olsson‡
† Division of Solid Mechanics, Lund University, P.O. Box 118, SE-221 00 Lund, Sweden
hakan.hallberg@solid.lth.se
‡ Materials Science and Applied Mathematics, Malmö University, SE-205 06 Malmö, Sweden
par.olsson@mah.se

Abstract

Microstructure evolution in thin Cu films during room temperature self-annealing is investigated by means of a mesoscale level set model. The model is formulated such that the relative, or collective, influence of anisotropic grain boundary energy, mobility and heterogeneously distributed stored energy can be investigated. Density functional theory (DFT) calculations are performed in the present work to provide the variation of grain boundary energy for different grain boundary configurations. The stability of the predominant (111) fiber texture in the as-deposited state is studied as well as the stability of some special low-Σ grain boundaries. Further, the numerical model allows tracing of the grain size distribution and occurrence of abnormal grain growth during self-annealing. It is found that abnormal grain growth depends mainly on the presence of stored energy variations, whereas anisotropic grain boundary energy or mobility is insufficient to trigger any abnormal growth in the model. However, texture dependent grain boundary properties, mobility in particular, contribute to an increased content of low-Σ boundaries in the annealed microstructure. The increased presence of such boundaries is also promoted by stored energy variations. In addition, if the stored energy variations are sufficient the coexisting (111) and (001) texture components in the as-deposited state will evolve into a (001) dominated texture during annealing. Further, it is found that whereas stored energy variations promote the stability of the (001) texture component, anisotropic grain boundary energy and mobility tend to work the other way and stabilize the (111) component at the expense of (001) grains.

Keywords: Grain growth, Texture, Cu, Thin film, Microstructure, Annealing, Recovery, DFT, Level set

DOI: 10.1016/j.jmps.2016.02.026

1 Introduction

Copper is commonly used for electrical wiring in integrated circuits by deposition of thin Cu films. However, such electroplated films may be considered to have a metastable microstructure directly following the deposition and significant changes to the material may occur through self-annealing, even at room temperature. The self-annealing is characterized by abnormal grain growth and can proceed for a duration of hours or weeks after the deposition [1, 2, 3, 4]. As this process involves extensive alterations of the microstructure in the film, also bulk thermomechanical and electrical properties of the film are changed. Most notably, the self-annealing process causes substantial changes in electrical resistivity [4, 5], crystallographic texture [6, 7, 8, 9, 10, 11], grain size and grain size distribution [3, 12, 4, 9, 13] as well as residual stress distribution [14, 7]. These microstructure changes will also have a secondary influence, for example since an increased grain size tends to mitigate processes such as electromigration [9]. Observations such as these have attracted significant research interest towards the process of self-annealing in thin Cu films. Despite this research effort, now spanning decades, there is still some dispute on the origins of the process and on the actual driving forces and microstructure mechanisms that are involved. While quite substantial experimental work has been done on the subject, considerably less work has been done in terms of developing models and numerical simulation techniques that can be used to further investigate and explain - and also to predict - the microstructure evolution during self-annealing in thin Cu films. Such numerical modeling is in focus of the present study. In passing, it can also be noted that the self-annealing is not limited to planar films, but also extends into interconnect lines in damascene trenches and vias found in integrated circuits [15, 16]. This further emphasizes the importance of the subject for different applications.

Surprisingly few studies have been published on numerical modeling of self-annealing processes in thin films. One example is given in [17], where a 2D model of grain growth in a generic thin film is considered. Grain growth stagnation related to thermal grooving is discussed and abnormal grain growth is triggered by artificially assigning different properties to different grains. The influence of crystallographic texture on the grain growth process is, however, not included in the model. Grain growth in thin films is also modeled in [2], using a 2D vertex-type (a.k.a. front-tracking) modeling approach. The numerical model considers the evolution of (111) and (001) textures.

Although some numerical models consider anisotropy of interface energies to some extent, the anisotropy of grain boundary mobility is usually not included. This is in spite of experiments highlighting that grain growth will take place as a highly orientation-dependent, i.e. anisotropic, process during self-annealing in Cu thin films [18]. The need for heterogeneous grain boundary mobility is also emphasized in, e.g., [19]. The relative influence on microstructure evolution by anisotropic grain boundary energy and mobility is considered in the present study. In addition, as noted in [19], it is likely that other driving forces need to be active in the microstructure for any significant self-annealing to take place at room temperature.

Hence, also the influence of heterogeneously distributed stored energy is accounted for here.

In the present study, the relative influence of anisotropic grain boundary properties and stored energy heterogeneities on microstructure evolution is in focus. It is therefore of interest to determine the magnitudes of the minimum grain boundary energies that can be found for a number of frequently occurring CSL configurations, such as coherent $\Sigma 3$ boundaries. *Ab-initio* calculations by density functional theory (DFT) are performed as part of the present work to determine the energies of a number of relevant low-Σ grain boundaries. To verify the validity of the calculated energies, the DFT results are compared to data reported in other publications. Mobilities for different grain boundary configurations are in the present model based on the increased mobility which is observed for high-angle boundaries in general and for $\Sigma 7$ and $\Sigma 13$b boundaries in particular.

The paper begins in Section 2 with an overview of self-annealing in thin Cu films and the microstructure processes that are involved. Mesoscale kinetics of grain growth are discussed in Section 3, where the coincidence site lattice (CSL) concept to characterize grain boundaries is outlined and anisotropy in terms of grain boundary energy and mobility is introduced. Evaluation of the variation of grain boundary energy with grain boundary configuration by *ab-initio* density functional theory calculations are performed in Section 4, later used as input for the mesoscale simulations in the present study. The mesoscale modeling of grain growth by the present finite element-based level set formulation is introduced in Section 5 and numerical simulations are performed in Section 6 along with a discussion on the results. Finally, some concluding remarks are provided in Section 8.

2 Self-annealing in Cu thin films

2.1 The as-deposited state

Deposition of thin Cu films is mainly done by electroplating as this method has been found to be superior to, e.g., chemical or physical vapor deposition in filling submicron trenches and vias in damascene architectured substrates [9]. After deposition, the Cu film has an equiaxed grain structure with an average grain size in the order of 0.050-1 μm [4, 9, 20]. Depending on the deposition process, a number of grains may initially be present throughout the thickness of the as-deposited film. However, a columnar grain structure tends to rapidly develop to provide a quasi-2D grain structure in the plane of the film. The initial grain structure is also influenced by any presence of impurities such as additives in the plating bath [9]. The initial grain size tends to decrease significantly with increasing impurity content due to boundary pinning [20]. Such grain boundary pinning results in an initial grain size that is approximately of the same thickness as that of the film.

Thin polycrystalline Cu films often have a texture where the (111) planes are aligned parallel to the plane of the film as the (111) orientations correspond to the lowest interface energy in face-centered cubic metals [6, 7]. Hence, this kind of (111) fiber texture will dominate in the as-deposited state [9].

The as-deposited film may be under a state of stress, which is usually of two different origins: *intrinsic stress* due to the growth of the film itself and *thermal stress* caused by the difference in thermal expansion between the film and the substrate onto which it is deposited [21, 14, 7]. Considering Cu deposition on Cu substrates, the thermal strains do not play a part [1].

There is evidence that the as-deposited microstructure in thin metallic films corresponds to that of a cold worked state in terms of stored energy [22]. As this stored energy can be expected to be heterogeneously distributed in polycrystalline thin films, cf. [7], this is one possible reason for the abnormal grain growth that is observed during self-annealing.

After deposition, the microstructure evolution in thin metallic films will proceed by the same processes that take place in the bulk material, i.e. through recovery, grain growth and recrystallization [23, 19]. However, the selection of favored grains during abnormal grain growth can be defined in terms of two selection criteria: a *thermodynamics-based criterion*, considering heterogeneous distributions of grain growth driving forces, and a *kinetics-based criterion*, considering anisotropy of grain boundary mobility [19]. Both of these criteria are considered in the present study as anisotropic grain boundary energy and mobility, as well as heterogeneously distributed stored energy, are considered.

2.2 Microstructure mechanisms involved in the self-annealing

Following deposition, an initial incubation period takes place which usually lasts for a few hours at room temperature. It is suggested in [4] that diffusion of pinning particles along the grain boundaries takes place during the incubation period and that Ostwald ripening results in a reduced pinning of the boundaries, permitting grain growth. This is, however, disputed in [24] where experiments indicate impurity redistribution to be a result of the grain growth rather than the other way around. The importance of impurities is also disputed in [19] where it is suggested that small enough initial grain size alone will trigger grain growth and that pinning effects do not contribute to the phenomena of self-annealing. Supporting the idea in [4], an incubation time during which impurity diffusion occurs towards the film surface, and while grain growth is inhibited, is identified in [25]. The impurity diffusion at room temperature can be expected to depend on the stress state, where a higher stress would increase impurity redistribution by stress-driven diffusion [25]. However, the incubation time seems to decrease with increasing film thickness, as noted in [5]. At film thicknesses below 0.4 μm, self-annealing has been shown to be suppressed completely [18].

After the incubation period, a transient phase enters during which abnormal grain growth takes place along with an evolution of texture, preferably promoting (111) or (100) fiber textures, to provide a final grain size in the order of a few microns [4, 9]. The transient time decreases with increasing film thickness [4]. During the transient phase, grain growth does not only alter the average grain size, but may also change the grain size distribution to provide a log-normal, possibly bimodal, grain size distribution [7]. Different texture components are found to be promoted, depending on the origin of the driving force for grain growth [2].

Increased film thickness and a higher stored energy emphasizes growth of the (001) texture component, while minimization of interface energies promote presence of the (111) texture component. Film thickness and stored energy can by these observations be expected to influence the texture evolution. The annealing temperature is also an important parameter and, as noted in [26], an increased annealing temperature tends to aid preferential growth of the (001) texture component. In [9], it is indicated that the as-deposited (111) texture becomes increasingly randomized during the annealing. This trend is also observed in [18], where the volume fraction of (111) fiber texture decreases during self-annealing while the volume fraction of (100) fiber texture increases. After approximately 50 days the two volume fractions seem to saturate at the same level of roughly 10 %. A reduced presence of (111) texture and an increased presence of (200) texture is observed when self-annealing is allowed to continue for more than 100 days, as seen in the study in [27]. In these experiments, it is also seen that the current density during plating has a very strong impact on the persistence of the (111) texture. The volume fraction of (111) texture is much more stable in films deposited using low plating current densities (3-5 $\mathrm{mA/cm^2}$) compared to high current densities (20-40 $\mathrm{mA/cm^2}$). Further, it is noted in [28] that the texture of the sputtered seed layer has a pronounced impact on the texture of the as-deposited film. This is also observed in [29], where the deposited film largely inherits the texture in the seed layer formed by physical vapor deposition. The observations made in the aforementioned studies on the stability of different texture components are in contrast to the ones made in [30], where the (111) texture becomes increasingly pronounced. To further complicate the picture, it can be noted that observations have been made in [31] of evolution of (110) and (311) textures in Cu thin films several days or months after deposition.

As a final stage, stagnation takes place and the microstructure evolution stabilizes. A saturation grain size is found in [13] as impurities gradually accumulate at the grain boundaries and in the limit prevent further grain boundary migration. Such a saturation of the self-annealing process can also be observed as a reduced rate of resistivity decrease with increasing annealing time, as shown in [1, 12, 5, 13, 25]. In [25], this saturation is found to occur approximately after 40 hours, beginning with a 1 μm film thickness and an initial grain size of 0.1 μm. Grain growth stagnation can occur, e.g., due to thermal grooving [32, 33] or grain boundary pinning [13, 34]. In addition, recovery will eventually reduce the stored energy levels below the critical threshold values needed to drive grain boundary migration.

3 Mesoscale grain growth kinetics

Let m and p denote the grain boundary mobility and the driving pressure, acting on the grain boundary, respectively. Then the local migration velocity v of a grain boundary can be written generally as

$$v = mp \tag{1}$$

If a stored energy jump $[\![E_\mathrm{s}]\!]$ is present across the boundary, the driving pressure p can be written as

$$p = p_\mathrm{E} + p_\gamma \quad \text{where} \quad p_\mathrm{E} = [\![E_\mathrm{s}]\!] \quad \text{and} \quad p_\gamma = -\kappa\gamma \tag{2}$$

where the local grain boundary curvature κ and the grain boundary energy γ were also introduced. The jump in stored energy is directly related to the difference or jump in dislocation density ρ_d across the grain boundary, providing

$$[\![E_\mathrm{s}]\!] = \tau[\![\rho_\mathrm{d}]\!] \tag{3}$$

where the dislocation line tension is given by $\tau = \mu b^2/2$, with b and μ denoting the magnitude of the Burgers vector and the shear modulus, respectively. These parameters are defined in relation to the numerical simulations in Section 6.

In the present study, both m and p will be considered as anisotropic quantities, depending on the local grain boundary character. This character will be defined in terms of CSL correspondence, which is discussed in the following subsection. Directly following that, the anisotropy of grain boundary energy and mobility is described in subsequent subsection.

3.1 CSL characterization of grain boundaries

Comparing the orientations of two adjacent crystals in a polycrystal, a number of atomic lattice sites may coincide in the two lattices. Such configurations are commonly denoted as *Coincidence Site Lattices*, CSL, providing grain boundaries that may have significantly different properties compared to general high-angle boundaries. The CSL boundaries are typically of low energy and high mobility. The type of CSL boundary is determined by Σ, where $1/\Sigma$ is the fraction of lattice sites that coincide.

Since the crystal orientations depend on three independent parameters, here taken as the Bunge-Euler angles $(\varphi_1, \Phi, \varphi_2)$, ideal CSL boundary configurations are scarce in real polycrystals. By the Brandon criterion, the range of misorientation angles $\Delta\theta_\Sigma$ that correspond to a certain CSL configuration is widened [35]. The Brandon criterion can be stated as

$$\Delta\theta_\Sigma = \frac{\theta_\Sigma}{\Sigma^{1/2}} \tag{4}$$

In eq. (4), the parameter θ_Σ determines the range of misorientation angles belonging to each CSL and usually $\theta_\Sigma = 15^\circ$ is chosen. This value is also adopted in the present work.

Letting $\boldsymbol{g}\,(\varphi_1, \Phi, \varphi_2)$ denote the orthogonal rotation matrix for a crystal, bringing the sample reference frame in alignment with the crystal reference frame, the misorientation between two crystals of rotations $\boldsymbol{g}_i$ and $\boldsymbol{g}_j$ can be written as $\Delta\boldsymbol{g}_{ij} = \boldsymbol{g}_j\boldsymbol{g}_i^\mathrm{T}$. The misorientation is then taken as the rotation which rotates one crystal reference frame into that of another.

In cubic materials, such as Cu, there exist 24 equivalent orientations for each crystal orientation $\boldsymbol{g}$. Following the usual approach, the minimum misorientation provided by these crystallographically equivalent configurations is taken as a measure of the misorientation.

This reduces the span of misorientation angles and the minimum misorientation is found by performing the minimization

$$\theta = \min_{\boldsymbol{O}_\mathrm{s} \in \mathcal{G}_\mathrm{c}} \left| \mathrm{acos} \left[\frac{1}{2} \left\{ \mathrm{tr} \left(\boldsymbol{O}_\mathrm{s} \Delta \boldsymbol{g} \right) - 1 \right\} \right] \right| \tag{5}$$

where the indices i and j were dropped for convenience and where $\boldsymbol{O}_\mathrm{s}$ is one the 24 operators in the cubic symmetry group $\mathcal{G}_\mathrm{c}$. The absolute value $|\cdot|$ is taken in eq. (5) to reflect that a negative angle simply indicates that the rotation axis points in the opposite direction. In eq. (5), the trace of a tensor is denoted by $\mathrm{tr}(\cdot)$. By performing a crystal symmetry reduction according eq. (5), a maximum misorientation of 62.8° can be expected in cubic crystal structures [36].

To determine the CSL correspondence of a particular grain boundary configuration according to the Brandon criterion, it is necessary to consider all possible symmetries related to the present misorientation $\Delta \boldsymbol{g}$. The symmetries of both grains, constituting the interface, need to be applied as well as the switching symmetry $\Delta \boldsymbol{g}_{ij} = \Delta \boldsymbol{g}_{ji}$. Also the rotation axis is considered to verify if it resides in the fundamental zone, i.e. in the standard stereographic triangle, or not. The corresponding scalar misorientation is usually referred to as the *disorientation* [37]. The disorientation is in the present work used together with eq. (4) to identify CSL boundaries.

3.2 Anisotropic grain boundary energy and mobility

Anisotropy of the grain boundary energy γ is commonly considered in mesoscale modeling of polycrystals by employing the classical Read-Shockley relation

$$\gamma_\mathrm{RS} \left(\theta \right) = \begin{cases} \gamma_\mathrm{m} \dfrac{\theta}{\theta_\mathrm{m}} \left[1 - \ln \left(\dfrac{\theta}{\theta_\mathrm{m}} \right) \right] & \text{if} \quad \theta < \theta_\mathrm{m} \\ \gamma_\mathrm{m} & \text{if} \quad \theta \geq \theta_\mathrm{m} \end{cases} \tag{6}$$

where θ_m is the angle that differentiates between low- and high-angle boundaries, defined by the disorientation angle θ. The usual choice of $\theta_\mathrm{m} = 15°$ is adopted here. In addition, γ_m is the grain boundary energy for general high-angle boundaries. According to eq. (6), a gradually increasing energy is modeled for low-angle boundaries whereas a constant energy is assumed for all high-angle boundaries.

The Read-Shockley relation is based on the idea of viewing low-angle boundaries as composed of dislocation planes inserted between the adjoining crystals. The misorientation of low-angle boundaries will be proportional to a multiple of the Burgers vector $\boldsymbol{b}$. By similar geometrical considerations, also high-angle CSL boundaries can be constructed by insertion of additional dislocation planes with a spacing proportional to $\boldsymbol{b}/\Sigma$, cf. [38]. Following this reasoning, the variation in boundary energy due to any CSL correspondence can be added to the Read-Shockley relation in eq. (6). The variation of grain boundary energy with CSL type

is provided by

$$\gamma_{\mathrm{CSL}}(\theta) = \begin{cases} -\frac{\tilde{\gamma}_\Sigma}{\Sigma}\left[1 - \frac{\Delta\theta}{\Delta\theta_\Sigma}\left(1 - \ln\left\{\frac{\Delta\theta}{\Delta\theta_\Sigma}\right\}\right)\right] & \text{if} \quad \Delta\theta < \Delta\theta_\Sigma \\ 0 & \text{if} \quad \Delta\theta \geq \Delta\theta_\Sigma \end{cases} \tag{7}$$

In eq. (7), the deviation from ideal CSL configurations is described by $\Delta\theta$ and the parameter $\tilde{\gamma}_\Sigma$ controls the magnitude of the reduction in grain boundary energy for a certain CSL type. For any disorientation, the variation in boundary energy with local grain boundary character is now provided by eqs. (6) and (7) as

$$\gamma(\theta) = \gamma_{\mathrm{RS}} + \gamma_{\mathrm{CSL}} \tag{8}$$

also considered in [39, 40, 41].

The grain boundary mobility will vary with the local grain boundary character in terms of misorientation across the boundary together with the inclination of the boundary plane and also due to the local content of solute atoms. Following [42], the essential characteristics of a low mobility for low-angle boundaries and a high mobility for high-angle boundaries can be estimated by adopting a disorientation dependence of the grain boundary mobility according to

$$m_\theta(\theta) = m_{\mathrm{m}}\left[1 - \exp\left(-5\left\{\frac{\theta}{\theta_{\mathrm{m}}}\right\}^4\right)\right] \tag{9}$$

where m_{m} is the mobility for general high-angle boundaries, which is held constant under the present isothermal conditions, and θ_{m}, like in eq. (6), is the angle that separate low- and high-angle boundaries.

As with grain boundary energy, also the grain boundary mobility may exhibit considerable variations with local grain boundary character. It can, for example, be noted that $\Sigma 7$ and $\Sigma 13$b tilt boundaries - corresponding to 38.2° and 27.8° rotation around the $\langle 111 \rangle$ axis, respectively - exhibit a significantly increased mobility [43, 44, 45, 46]. To allow for such locally increased mobility in the present model, a CSL-dependent component is added to eq. (9), inspired by eq. (7), according to

$$m_{\mathrm{CSL}}(\theta) = \begin{cases} \frac{\tilde{m}_\Sigma}{\Sigma}\left[1 - \frac{\Delta\theta}{\Delta\theta_\Sigma}\left(1 - \ln\left\{\frac{\Delta\theta}{\Delta\theta_\Sigma}\right\}\right)\right] & \text{if} \quad \Delta\theta < \Delta\theta_\Sigma \\ 0 & \text{if} \quad \Delta\theta \geq \Delta\theta_\Sigma \end{cases} \tag{10}$$

where the parameter $\tilde{m}_\Sigma$ permits scaling of individual CSL boundary mobilities. Combining eq. (9) and eq. (10), the grain boundary mobility is in the present model determined for individual grain boundary segments from

$$m(\theta) = m_\theta + m_{\mathrm{CSL}} \tag{11}$$

Settings of the grain boundary parameters related to energy and mobility are discussed further in relation to the numerical simulations in Section 6.

Through the model outlined above, anisotropic grain boundary properties are currently assumed to depend only on the local disorientation between neighboring grains. A full description of a grain boundary configuration should ideally consider not only the three orientation parameters for each crystal, but also two parameters to define the inclination of the boundary plane. However, according to [39], the influence of boundary plane inclination is likely to be minor. In addition, several authors note that evolution of grain boundary texture can be expected also when adopting a disorientation-based anisotropy of grain boundary properties [47, 48, 49, 50, 51, 39].

4 Evaluation of grain boundary energies by ab-initio calculations

Density functional theory (DFT) calculations are performed as part of the present work in order to estimate the grain boundary energy for a number of low-energy CSL configurations that are likely to be present and influence the microstructure evolution. These low energy configurations can be expected to be more stable than other random high-angle grain boundaries and also to occur more frequently as the annealing process proceeds.

In order to compute the grain boundary energies using DFT, calculations of the ground state energy for atomic configurations containing grain boundary interfaces are performed. The grain boundaries were generated using the open-source GBSTUDIO software [52], which has the capability to generate atomic grain boundary configurations that satisfy periodic boundary conditions in 3D. Thus, because each simulation supercell contains two grain boundaries, the grain boundary energy can be computed as

$$\gamma = \frac{E_{\mathrm{gb}}^{N} - N E_{\mathrm{b}}}{2A} \tag{12}$$

where E_{gb}^{N} is the ground state energy for an atomic grain boundary configuration containing N atoms, E_{b} is the cohesive energy and A corresponds the grain boundary area. The factor of two in the denominator of eq. (12) emerges because of the fact that the supercell contains two grain boundaries.

Low Σ-grain boundaries are considered with the misorientation axis $[1\bar{1}0]$, for which the misorientation angles lie in the interval $38.9^\circ \leq \theta \leq 141.1^\circ$. To ensure that the lowest energy configurations are obtained, in addition to considering symmetric tilt grain boundaries, neighboring grains are also sheared such that one of them are subjected to a rigid body translation. Thus, the atomic positions are allowed to relax from different initial configurations, such that relative displacements following grain boundary sliding are accounted for. Moreover, to prevent numerical issues resulting from very closely positioned atoms, neighboring atoms in the initial configuration are merged if the interatomic distance is less than 40% of the lattice parameter.

All DFT simulations in this work are performed using the well-established Vienna *ab initio* simulation package (VASP) [53, 54, 55, 56]. For modeling the electron-ion interaction the frozen core projector-augmented-wave method is adopted, cf. [57, 58], with the valence electron description for Cu comprising the $3d^{10}4s^1$ orbitals. The employed electron-electron exchange-correlation functional is described within the generalized gradient approximation on the format corresponding to that proposed by Perdew, Burke and Ernzerhof [59, 60]. The atomic site optimizations are performed using a quasi-Newton algorithm [61] during which no relaxation of the supercell size or shape is allowed.

In order to obtain satisfactory results the kinetic energy cutoff for the plane-wave basis set and k-point density is converged such that the ground state energy is within 1.0 meV/atom. To achieve this, a kinetic energy cutoff corresponding to 403 eV and a Monkhorst-Pack k-point grid of size $16 \times 16 \times 16$ for the primitive cell of FCC Cu were used [62]. The k-point grids for the reciprocal grain boundary supercells are made commensurate with the k-point density of the primitive FCC cell. In order to prevent numerical issues associated with lack of convergence from occurring, smearing of the Brillouin zone integration is used based on the Methfessel-Paxton scheme [63]. The adopted smearing width used in the calculations corresponds to a broadening of 0.1 eV, which was found to give satisfactory convergence and sufficient accuracy in the calculations.

4.1 Resulting grain boundary energies

Table 1 summarizes the calculated grain boundary energies. In order to minimize the grain boundary energy, in addition to completely symmetric atomic configurations also grain boundary planar shifts were performed. For some cases such shifts resulted in lowering of the grain boundary energy. For instance, for the $\Sigma9(114)[1\bar{1}0]38.9^\circ$ and $\Sigma3(112)[1\bar{1}0]70.5^\circ$ grain boundaries it was observed that a shift in the direction of the misorientation axis of half the interplanar distance is energetically favorable, cf. Fig. 2. For the $\Sigma9(221)[1\bar{1}0]141.5^\circ$ grain boundary there is a slight distortion in the lattice with a minor shift in the $[11\bar{4}]$-direction which results in a deviation from the perfect mirror symmetry. Combined with the merging of two closely situated atoms in the proximity of the grain boundary, this led to a reduction in the grain boundary energy from 1.20 J/m^2 for the perfect mirror symmetry system to 0.80 J/m^2 for the distorted and reduced system. This result concurs with the findings based on semi-empirical modeling in [64].

The results in Table 1 concur well with results obtained from classical atomistic simulations based on semi-empirical embedded atom method (EAM) potentials [66, 65]. Most notably it is seen that the predicted universal grain boundary energy curve for FCC metals, parametrized by Bulatov *et al.* [65], is well represented by the DFT calculated grain boundary energies of this work, as illustrated in Figure 1. The only exception for which there is a notable deviation

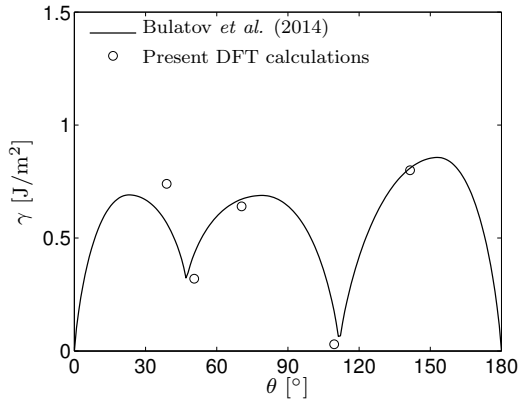

Figure 1: Comparison between DFT computed grain boundary energies (circles) and the parametric fit of Bulatov *et al.* [65] (solid lines) for the misorientation axis $\langle 1\bar{1}0\rangle$.

Table 1: Grain boundary energy, γ, for a number of low Σ-grain boundaries in Cu, calculated in the present work using DFT.

Boundary	γ [J/m^2]
$\Sigma9(114)[1\bar{1}0]38.9^\circ$	0.74
$\Sigma11(113)[1\bar{1}0]50.5^\circ$	0.32
$\Sigma3(112)[1\bar{1}0]70.5^\circ$	0.64
$\Sigma3(111)[1\bar{1}0]109.5^\circ$	0.03
$\Sigma9(221)[1\bar{1}0]141.1^\circ$	0.80

is in the case of the $\Sigma9(114)[1\bar{1}0]38.9^\circ$ grain boundary for which the predicted *ab-initio*-data is about 20 % higher than that found in [65] based on EAM formalism. To investigate this closer we applied relative shifts in the $[1\bar{1}0]$- and $[22\bar{1}]$-directions. However, no reduction in the grain boundary energy was observed. This could be attributed to that we have prohibited relaxation of the simulation cell in the out-of-plane direction. Nevertheless, for the task at hand the obtained accuracy of the grain boundary energies is satisfactory. The low energy associated with the $\Sigma3(111)[1\bar{1}0]109.5^\circ$ grain boundary is attributed to the fact that it is a symmetric $\Sigma3(111)[111]60^\circ$ twist boundary, which corresponds to a highly symmetric and coherent twin boundary. The calculated value of about 30 mJ/m^2 concurs well with the experimental data of 24 mJ/m^2 [67].

5 Level set formulation of grain growth in polycrystalline aggregates

Since introduced in [68], the level set method has been employed in numerous studies to trace the evolution of interfaces in quite arbitrary physical settings. The present level set implementation follows that in [69] and similar formulations can also be found in [70, 71, 72]. The level set framework employed in the present study is briefly summarized in this section for completeness and in order to identify components that are of importance here.

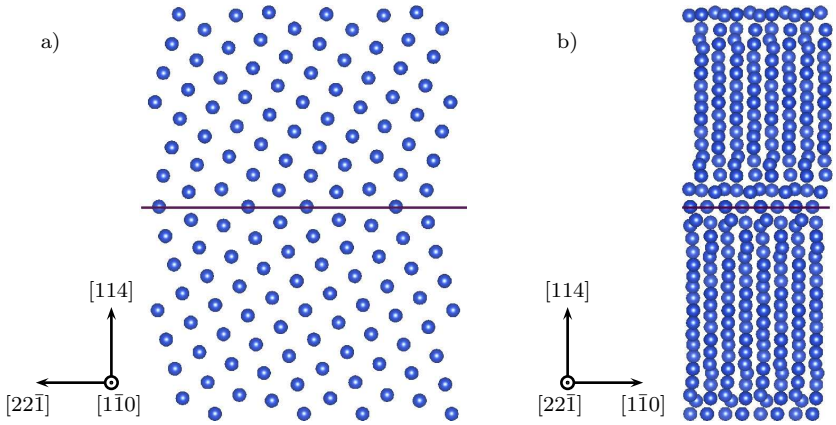

Figure 2: Illustration of a $\Sigma 9(114)[1\bar{1}0]38.9°$ grain boundary. a) View in the direction of the misorientation axis. b) Illustration of the relative displacement between the top and bottom grains, perpendicular to the misorientation axis. The solid horizontal lines correspond to the location of the grain boundary.

Let the level set function $\phi(\boldsymbol{x},t)$ be defined on a domain Ω, where $\boldsymbol{x}$ are the spatial coordinates and t the time. The zero-level contour where $\phi = 0$ is taken to represent the spatial discontinuity Γ, i.e. the interface. Further, the level set function is defined as a distance function, for any point $\boldsymbol{x}$ representing the distance $d(\boldsymbol{x},t,\Gamma)$ to the interface Γ at a certain time. In addition, a sign convention is adopted whereby it holds that $\phi > 0$ inside Γ, $\phi < 0$ outside of the interface and $\phi = 0$ at the interface. These preliminaries provide

$$\begin{cases} \phi(\boldsymbol{x},t) = d\left(\boldsymbol{x},t,\Gamma\right), \ \boldsymbol{x} \in \Omega \\ \Gamma = \{\boldsymbol{x} \in \Omega, \ \phi(\boldsymbol{x}) = 0\} \end{cases} \tag{13}$$

Since $\phi(\boldsymbol{x},t)$ is taken as a signed distance function, it also holds that

$$\|\boldsymbol{\nabla}\phi(\boldsymbol{x},t)\| = 1, \quad \boldsymbol{x} \in \Omega \tag{14}$$

The local interface normal $\boldsymbol{n}$ and the interface curvature κ can be evaluated directly from the level set function according to

$$\begin{cases} \boldsymbol{n} = \dfrac{\boldsymbol{\nabla}\phi}{\|\boldsymbol{\nabla}\phi\|} \equiv \boldsymbol{\nabla}\phi, \\ \kappa = \boldsymbol{\nabla}^{\mathrm{T}}\boldsymbol{n} \equiv \boldsymbol{\nabla}^{\mathrm{T}}\left(\dfrac{\boldsymbol{\nabla}\phi}{\|\boldsymbol{\nabla}\phi\|}\right) \equiv \boldsymbol{\nabla}^2\phi \end{cases} \quad \text{if} \quad \|\boldsymbol{\nabla}\phi\| = 1 \tag{15}$$

Differentiation of eq. (13) with respect to time provides the evolution law for the interface as

$$\frac{\partial\phi}{\partial t} + \left(\boldsymbol{\nabla}^{\mathrm{T}}\phi\right)\frac{\partial\boldsymbol{x}}{\partial t} = 0 \tag{16}$$

Generalizing this result to a situation with an arbitrary number of N_ϕ level sets provides

$$\begin{cases} \dfrac{\partial\phi_i}{\partial t} + \boldsymbol{v}^{\mathrm{T}}\boldsymbol{\nabla}\phi_i = 0, \\ \phi_i(t=0,\boldsymbol{x}) = \phi_i^0(\boldsymbol{x}), \end{cases} \quad \forall \ i \in \{1...N_\phi\} \tag{17}$$

where $\boldsymbol{v}$ denotes the local interface velocity vector and where $\phi_i^0(\boldsymbol{x})$ are the initial interface configurations at time $t = 0$.

When numerically evolving the interfaces, there is sometimes a tendency for the level sets to separate or overlap at interfaces. This is mitigated by performing an interaction correction step with some regularity during the course of the solution. There is also a tendency of the level sets to drift from maintaining the property of being signed distance functions when continuously evaluating eq. (17). This issue is remedied through reinitialization of the level set functions. Further details on the level set interaction correction and the reinitialization scheme are given in [69].

Considering level sets applied to modeling of grain growth, the interface velocity $\boldsymbol{v}$ appearing in eq. (17) is with eqs. (1) and (2) given by

$$\boldsymbol{v} = \boldsymbol{v}_\rho + \boldsymbol{v}_\kappa \tag{18}$$

where the velocity component $\boldsymbol{v}_\rho$, related to a stored energy jump between crystals i and j, is defined as

$$\boldsymbol{v}_\rho = v_\rho \boldsymbol{n} \quad \text{where} \quad v_\rho = m[\![E_\mathrm{s}]\!]_{ij} \tag{19}$$

The evaluation of the velocity component is based on the establishment of a velocity field, following the procedure outlined in [70, 69].

The velocity component $\boldsymbol{v}_\kappa$, related to grain boundary curvature, is found as

$$\boldsymbol{v}_\kappa = v_\kappa \kappa \boldsymbol{n} \quad \text{where} \quad v_\kappa = -m\gamma \tag{20}$$

If advantage is taken of eq. (15) and if it is assumed that $\|\boldsymbol{\nabla}\phi_i\| = 1$ holds due to level set reinitialization, then eq. (17) can be reformulated by insertion of the velocity components to provide

$$\begin{cases} \dfrac{\partial \phi_i}{\partial t} + \boldsymbol{v}_\rho^{\mathrm{T}} \boldsymbol{\nabla}\phi_i + v_\kappa \boldsymbol{\nabla}^2 \phi_i = 0, \\ \phi_i(\boldsymbol{x}, t = 0) = \phi_i^0(\boldsymbol{x}), \end{cases} \qquad \forall\ i \in \{1...N_\phi\} \tag{21}$$

The advection-diffusion system in eq. (21) is in the present implementation solved in a finite element setting. To consider the influence of anisotropic grain boundary properties in the numerical solution scheme, all elements containing interfaces are identified when assembling the element matrices in each solution step. Elements containing interfaces, being the zero-contour of any level set, are identified by evaluating $s_i = (\max \phi_i)\,(\min \phi_i)$ in each element for all $i = 1...N_\phi$ level sets. If $s_i \leq 0$, the element contains the interface of the corresponding level set ϕ_i. This approach also allows convenient identification of the level sets that meet in an individual element. Having identified the neighboring level sets, the interface properties can be evaluated according to Sections 3.1 and 3.2 to provide the correct values of the grain boundary mobility m and energy γ.

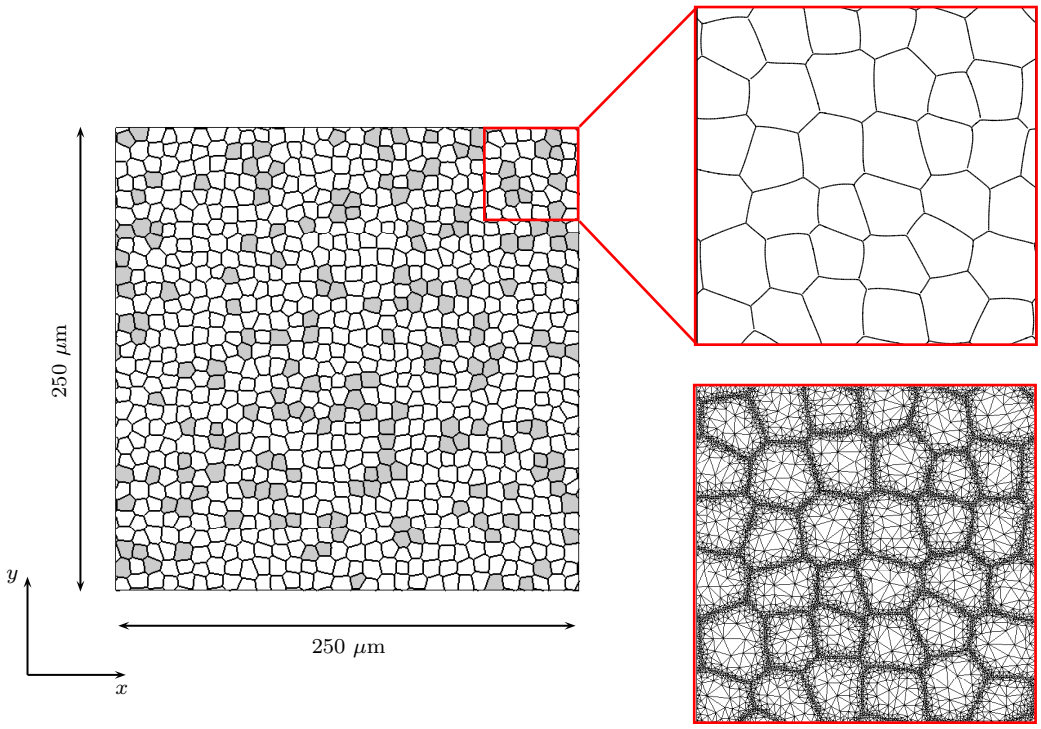

Figure 3: The initial 900 grain polycrystal used in the 2D mesoscale simulations. Grains with (111) texture are white and grains belonging to the (001) texture component are shaded gray. The inserts show a magnification of the grain boundary network and the finite element mesh discretization of the same region, respectively.

6 Numerical simulations

To perform the level set-based mesoscale simulations, a 2D polycrystal with 900 grains is considered as shown in Fig. 3 and material data pertaining to pure Cu is summarized in Table 2. This 2D microstructure is expected to be representative for the as-deposited Cu thin film after the initial incubation period according to the discussion in Section 2. The Cu film is assumed to have been deposited on a substrate of the same material, whereby thermal strains are neglected. The initial grain structure is generated by Voronoi tesselation, followed by isotropic curvature-driven grain growth until a representative grain structure with equilibrated grain boundary triple junctions is achieved. An initial grain size of approximately 10 μm is considered. A homogeneous grain size distribution, as seen in Fig. 3, is also observed in actual Cu thin films in [20].

Since the present level set formulation is employed in a finite element setting, the computational domain is discretized using triangular elements with linear interpolation, as illustrated in the bottom-right close-up in Fig. 3. Adaptive remeshing is used in each time step during the solution procedure to maintain proper mesh resolution along the grain boundary interfaces, i.e. the level set zero contours, achieved by a enforcing a condition on the maximum

Table 2: Material parameters pertaining to pure Cu at room temperature.

Parameter	Description	Value	Ref.
b	Magnitude of the Burgers vector	0.256 nm	[73]
μ	Shear modulus	42 GPa	[74]
γ_{m}	Grain boundary energy for general HAGB	0.744 J/m^2	[75]
m_{m}	Grain boundary mobility for general HAGB	7.1×10^{-16} m^4/Js	[19]

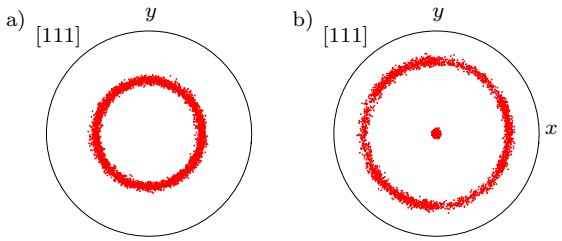

Figure 4: The [111] pole figures of the texture components initially present in the microstructure: a) Grains belonging of (001) type and, b), grains of the (111) texture component.

element size in such regions.

To allow tracing of the relative stability of (111) and (001) texture components, respectively, the individual grains in the 2D polycrystal are assigned orientations of either of the two types. The initial texture is assumed to be dominated by a (111) fiber texture as noted in [6, 2, 7, 9, 10, 20]. To represent this, 4/5 of the initial grains are set to be of the (111) type and 1/5 of the (001) type, randomly selected. The initial texture is generated by assigning an orientation to the individual grains in terms of the Bunge-Euler angles $(\varphi_1, \Phi, \varphi_2)$ with a 4° Gaussian spread around the ideal orientation, either (111) or (001). The [111] pole figures of the two texture components are shown in Fig. 4 and the distribution of grains from the two texture populations in the initial microstructure is shown in Fig. 3, where (001) grains are shaded gray.

The resulting grain boundary disorientations in the initial microstructure are illustrated in Fig. 5. Note that since cubic crystal symmetries are considered, the maximum disorientation that is encountered will be 62.8°.

As discussed in Section 2, many studies have been published on the mechanisms involved in room-temperature annealing of thin Cu films, not least on abnormal grain growth, e.g. [76, 77, 78]. Not surprisingly, a main conclusion from such studies is that a prerequisite for abnormal grain growth is a heterogeneously distributed presence in the microstructure of either driving forces and/or pinning features. The present level set model will in the following subsections be employed in studying the relative influence of anisotropic grain boundary energy, mobility and heterogeneously distributed stored energy on the microstructure evolution. As a reference, a

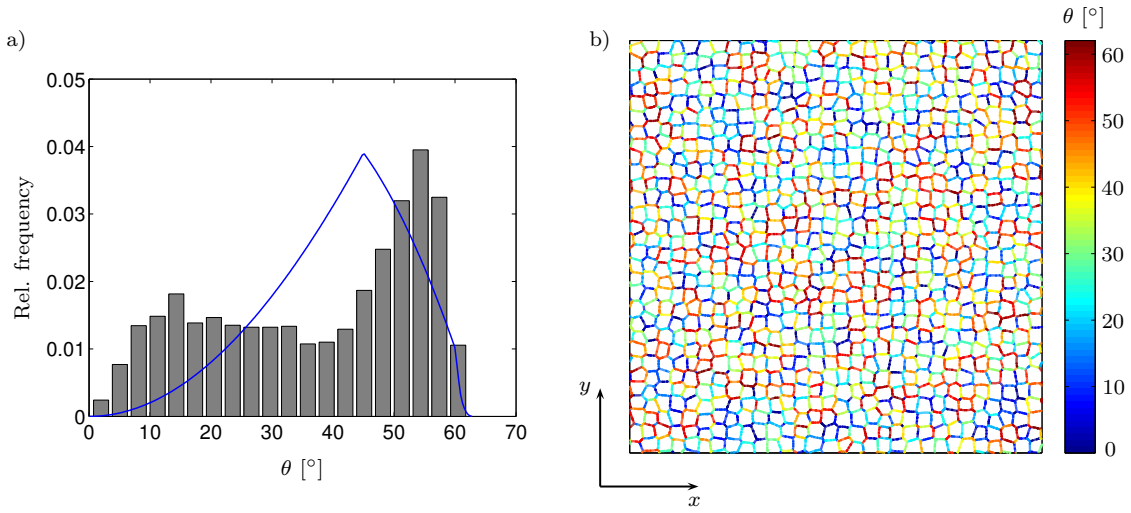

Figure 5: a) Disorientation distribution in the initial microstructure. The solid line indicates the Mackenzie distribution of disorientations in a randomly textured cubic polycrystal [36]. b) Disorientation along the grain boundaries in the initial microstructure. Note that due to consideration of cubic crystal symmetries, the maximum disorientation is 62.8°.

simulation is also run entirely isotropic, without any influence of texture or stored energy. All simulations are run for a total annealing time of 20 hours.

6.1 Influence of heterogeneously distributed stored energy

Dislocation mechanisms in thin films have been studied extensively using discrete dislocation dynamics, e.g. [79, 80]. In such studies it is noted that although the (100) and (111) components in thin films in principle only differ by the inclination of the (111) slip planes with respect to the plane of the film, significant differences in dislocation processes occur. The generation of dislocations and the presence of plastic strains in thin films is also discussed in, e.g., [23]. Further, from experiments on Cu thin films, performed in [81], it is noted that the flow stress and hardening rate is considerably higher in the (100) fiber than in the (111) fiber. This trend is also observed by x-ray diffraction studies on Cu thin films in [82] and from nanoindentation testing of thin films, performed in [83]. While differences in elastic energy are indeed a driving force for grain boundary migration, the driving force due to stored energy differences will be up to five orders of magnitude higher, cf. [41]. Significant stress levels have been measured in as-deposited thin films in a number of studies, e.g. [84, 85], well above the initial yield stress of Cu. This indicates that the microstructure is in a cold worked state, with a lower dislocation content in the (111) component than in the (100) component.

The initial dislocation density can be estimated from measurements of the yield stress σ_y of the as-deposited polycrystal film, by considering $\sigma_y = 0.5\mu b\sqrt{\rho_d}$. Considering the results in [85] on Cu thin films, compressive stresses in the order of -180 MPa can be expected in a deposited film of 1 μm thickness. Such stress corresponds to a dislocation density of about

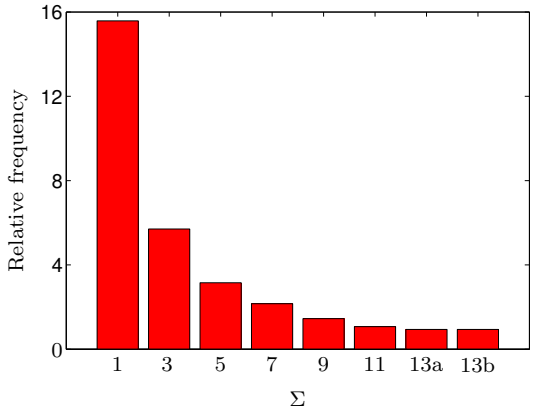

Figure 6: Distribution of low-Σ CSL boundaries, weighted by length, in the initial microstructure.

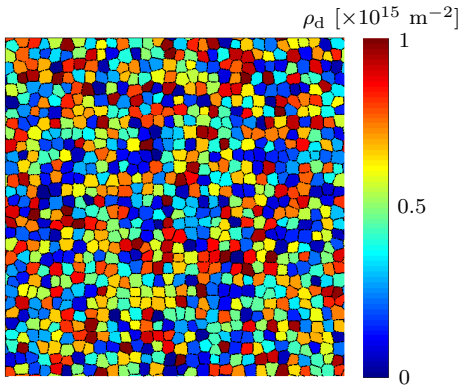

Figure 7: Distribution of dislocation density in the initial microstructure.

$\rho_d = 1.1 \times 10^{15}$ m^{-2}. In [4], it is noted how the stored energy present in the as-deposited film is removed after approximately 9 hour self-annealing at room temperature.

The (111) textured grains will be randomly assigned a dislocation density ρ_d from a normal distribution with a mean of 1×10^{15} m^{-2} and a standard deviation of 1×10^{14} m^{-2}. The (001) textured grains are assumed to have a significantly lower stored energy, for simplicity set to be one half of that of the (111) grains. The influence of varying the relative dislocation densities in the (111) and (001) grains is discussed in Section 7. The use of a normal distribution of stored energy is also considered in [7]. The initial dislocation density distribution in the microstructure presently under consideration is shown in Fig. 7.

6.2 Influence of anisotropic grain boundary mobility

Room temperature self-annealing in Cu films may last for days or weeks [1, 3, 4], much owing to the low mobility of grain boundaries in the material at this temperature, cf. Table 2. As data on grain boundary mobility in pure copper found in the literature shows great scatter,

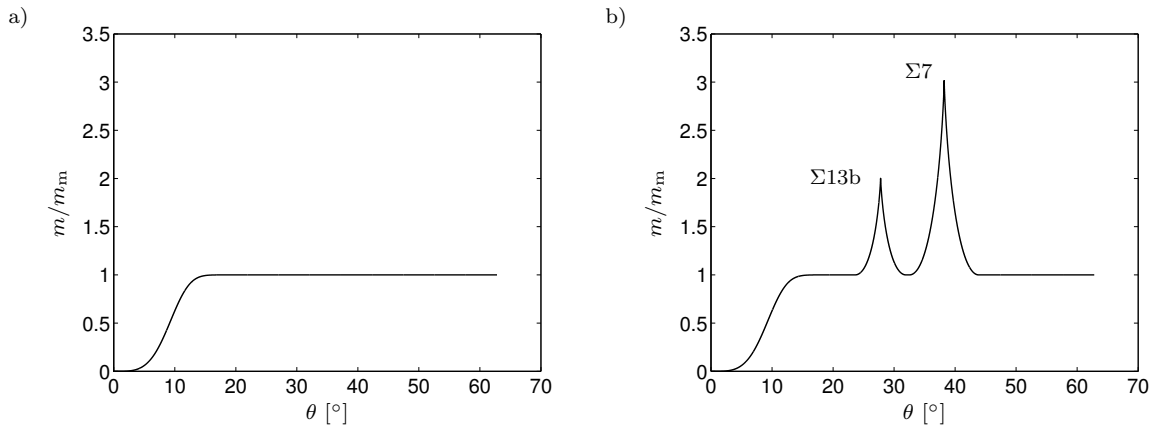

Figure 8: a) Variation of the grain boundary mobility due to eq. (9). b) Grain boundary mobility variation if the increased mobility of some characteristic low-Σ boundaries is considered according to eq. (11).

Table 3: Values of the grain boundary mobility scaling parameter $\tilde{m}_\Sigma$ used in the present model for high mobility CSL configurations.

CSL	$\tilde{m}_\Sigma$ [m^4/Js]
Σ7	1.0×10^{-14}
Σ13b	9.3×10^{-15}

the estimated mobility value should be taken with some caution. The value is, however, consistent with the very low grain boundary migration rates that are observed during room temperature annealing. The low migration rate strongly suggests that increased grain boundary mobility and reduced grain boundary energy must be present for certain grain boundary types, combined with a heterogeneous stored energy distribution, in order for abnormal grain growth to take place.

When it comes to anisotropy related grain boundary mobility, a differentiation between low-angle (low mobility) and high-angle (higher mobility) boundaries is achieved already by considering eq. (9), cf. Fig. 8a. However, as noted in the discussion related to eq. (10), it can be noted that, e.g., Σ7 and Σ13b tilt boundaries exhibit a much increased mobility [43, 44, 45, 46]. In [11], a corresponding increased presence of such boundaries is also observed during grain growth in Cu. Pronounced variations in grain boundary mobility in Cu are also found in [86], based on atomistic simulations of twist boundaries. To take the increased mobility of Σ7 and Σ13b boundaries into account, the grain boundary mobility scaling parameter $\tilde{m}_\Sigma$ in eq. (10) is set according to Table 3, to provide the mobility variation shown in Fig. 8b by using eq. (11). As an estimate, the mobility of Σ7 and Σ13b boundaries are taken as three times and twice, respectively, the mobility of general high-angle boundaries, cf. Fig. 8b.

Table 4: Values of the grain boundary energy scaling parameter $\tilde{\gamma}_\Sigma$ used in the present model for low energy CSL configurations.

CSL	$\tilde{\gamma}_\Sigma$ [J/m^2]
$\Sigma 3$	2.18
$\Sigma 9$	3.01
$\Sigma 11$	6.22

6.3 Influence of anisotropic grain boundary energy

As with grain boundary mobility, the grain boundary energy varies with grain boundary character both in terms of misorientation and by the inclination of the boundary plane. Adopting a CSL classification of "special" boundaries, it can be noted, however, that some CSL configurations show greatly reduced grain boundary energy. As an example related to Cu, it is noted in [67] that coherent $\Sigma 3$ boundaries may have a grain boundary energy that is only approximately 0.024 J/m^2 at 925 K, compared to 0.625 J/m^2 for general high-angle boundaries at the same temperature. These values agree well with the energy levels obtained from the present DFT calculations, stated in Table 1 and shown in Fig. 1. In the present study, advantage is taken of the grain boundary energy energies evaluated by DFT in Section 4. Considering the resulting grain boundary energy data, collected in Table 1, it can be noted that $\Sigma 3$, $\Sigma 9$ and $\Sigma 11$ boundaries exhibit considerable drops in the grain boundary energy, depending on the local grain boundary configuration. The present mesoscale model considers anisotropy in terms of local disorientation and CSL correspondence but does not, however, account for the inclination of the grain boundary plane. The energy values in Table 1 are thus taken as lower bounds, indicative of the energy minima that could possibly be encounter for certain CSL configurations. By this approach, and if the grain boundary energy scaling parameter $\tilde{\gamma}_\Sigma$, appearing in eq. (7), is set according to Table 4, the grain boundary energy variation shown in Fig. 9b is obtained from eq. (8).

7 Results

The results from the three simulation set-ups that were defined in Sections 6.1-6.3 and from the isotropic reference simulation are shown and discussed in this section.

The evolution of the average grain diameter d, normalized by its initial value d_0, is shown in Fig. 10a. The graphs are labeled in such way that "Isotropic" refers to the simulation where all properties are isotropic, "Stored energy" refers to the case where stored energy variations are present in the microstructure while "GB energy" and "GB mobility" relates to the respective cases where grain boundary energy and mobility are taken as anisotropic quantities. Related to the grain growth, the change in number of grains with increasing annealing time is shown in Fig. 10b. It can be noted that when considering anisotropic grain boundary energy or mobility,

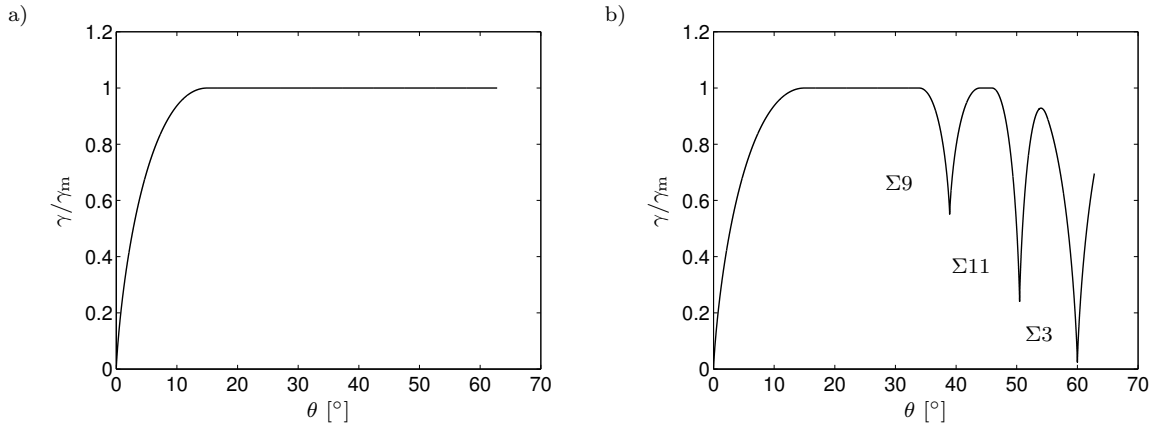

Figure 9: a) Variation of grain boundary energy according to the Read-Shockley relation, cf. eq. (6). b) Grain boundary energy variation considering some low-Σ configurations according to eq. (8).

both the grain growth behavior and the grain count follows closely what is obtained for the isotropic system. A significant difference is, however, seen as a stored energy distribution is considered among the grains that constitute the model microstructure, also cf. Fig. 7.

Focusing on the simulations with stored energy differences and looking at Fig. 10b, it can be seen that at the end of the considered 20 h annealing time, the number of grains in the polycrystal has dropped to approximately one third of the initial value. This is still a substantial number of grains and as seen in Figs. 12d and 14b, (111) grains are still present and grain growth driven by stored energy reduction is still taking place. The evolution of grain size, as seen in Fig. 10a, will gradually slow down and saturate, but at a later time, when only (001) grains remain and when normal - isotropic - grain growth kinetics alone govern the process.

Another view of the microstructure evolution is given by considering the grain size distribution, in each case normalized by the average grain size $\langle A \rangle$, as shown in Fig. 11. The initial grain size distribution (solid red line) indicates that all grains have similar size, as also seen in the initial microstructure in Fig. 3. A greater spread among the grain sizes is found in Fig. 11 at the end of the annealing period in the different cases. As no artificial grain growth stagnation condition is employed in the present model, the coexistence of growing and shrinking grains results in the wider final-state grain size distributions in Fig. 11 compared to the initial distribution. A notably different characteristic can be found in the case where stored energy variations are considered, where larger (001) grains are present together with gradually disappearing (111) grains. For the other simulation cases, the grains of the two texture components continue to be of nearly equal size. These observations become more evident as the relative presence of the (001) and (111) texture components is further discussed below. In all cases seen in Fig. 11, the grain size distributions are well described by a

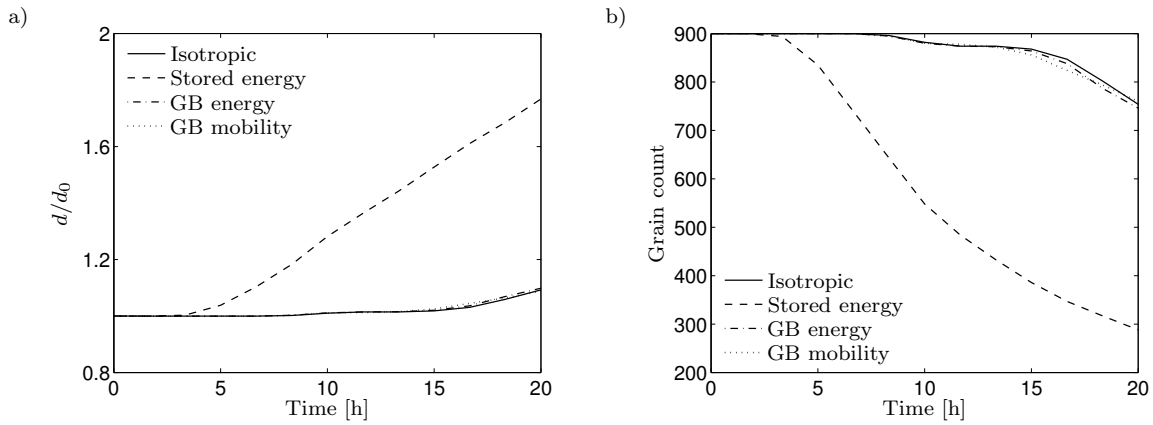

Figure 10: Influence of different simulation settings on: a) Evolution of the grain size and b) Evolution of the number of grains.

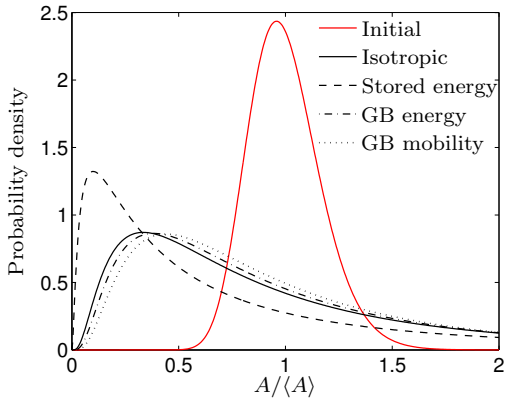

Figure 11: Grain size distribution, initially as well as at the end of the annealing period, with different simulation settings.

log-normal distribution function, as was also found in annealing experiments on Cu thin films in [7]. In addition, the distributions are also all monomodal which is in agreement with the experimental results on Cu thin films in [11].

The initial presence of the two texture components is shown in Fig. 3 where (001) crystals are shaded gray while the (111) crystals are white. The presence of the two texture components after annealing is shown in Fig. 12, which also shows the final grain structures from the different simulations. The relative presence of (111) and (001) grains is very similar in the case of an isotropic system, Fig. 12a, and when employing anisotropic grain boundary properties, Fig. 12b-c. A marked difference is seen in Fig. 12d where stored energy variations are considered. Most of the initial (111) grains have been consumed by growing (001) grains. The lower stored energy in the latter texture component has significantly promoted growth of such grains to an extent that might be viewed as abnormal growth of the (001) textured

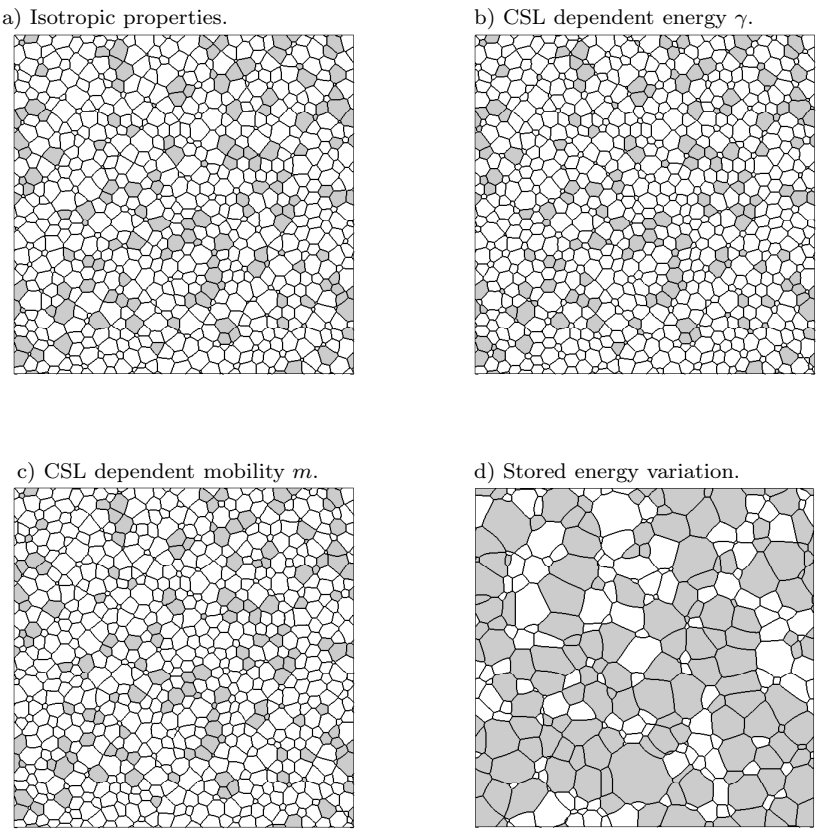

Figure 12: The final microstructure obtained under different simulation settings. The initial grain structure, used for all simulations, is shown in Fig. 3. a) Entirely isotropic system. b) Grain boundary energy varying according to Fig. 9b. c) Grain boundary mobility varying as in Fig. 8b. d) Isotropic system, but with different dislocation densities for the (111) and (001) grains, cf. Fig. 7.

crystals.

Not only the grain structure evolves during self-annealing, but also the texture. Fig. 13 shows the length-weighted distribution of the low-Σ boundary types that are considered in the present model. The initial distribution is repeated here from Fig. 6 to allow comparison with the distributions obtained at the end of the annealing period when considering the different model scenarios. During grain growth, a general tendency is an increased content of general low-angle boundaries as discussed in, for example, [87, 72]. This is also evident in the present case when looking at the $\Sigma 1$ content in Fig. 13, except for the case where stored energy variations are considered. In the latter case, the microstructure has evolved to contain a greater amount of $\Sigma 1$ boundaries as more and more grain boundaries separate crystals from the same (001) texture component, at the same time involving (111) crystals to a lesser extent. While the fraction of general $\Sigma 1$ boundaries is reduced, the content of $\Sigma 3$, $\Sigma 5$, $\Sigma 7$ and $\Sigma 9$ increases which can be seen as a tendency towards formation of a microstructure with a lesser degree

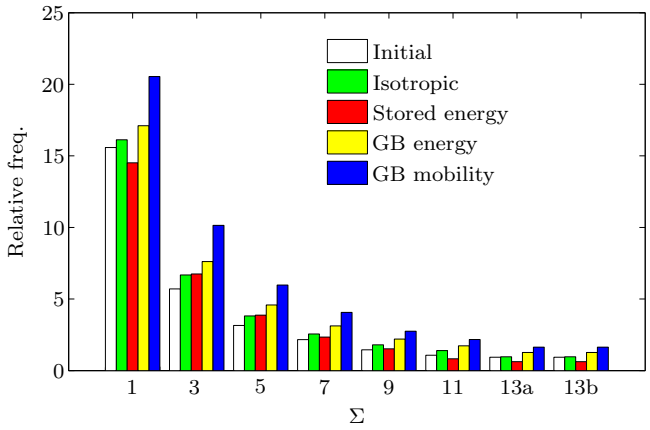

Figure 13: Distribution of low-Σ boundaries, initially, as well as at the end of the simulations, using different simulation settings.

of texture randomization. Looking at the cases where anisotropic grain boundary properties are considered, it can be noted that anisotropic grain boundary mobility in particular tends to strengthen the presence of low-Σ boundaries. Looking at the adopted mobility variation, shown in Fig. 8b, the influence would be greatest for Σ7 and Σ13b boundaries. But the narrow width of the mobility peaks in Fig. 8b is likely to be too restrictive as very few boundaries will satisfy the disorientation criterion to achieve the maximum mobility. Turning to the influence of anisotropic grain boundary energy, the energy minima are found for boundaries of the Σ3, Σ9 and Σ11 types, cf. Fig. 9b. As seen in Fig. 13, the content of these boundaries increase as anisotropic grain boundary energy is considered. However, as with the mobility, there are too few boundaries that fit the criterion to achieve minimum energy to give clear impact on the content of the respective type of boundary. These observations are in line with what was found in [72] for grain growth in the general anisotropic case.

The area fractions of the (111) and (001) texture components during annealing are shown in Fig. 14 for the different simulation cases. The graphs in Fig. 14 are consistent with the previous observations of coexistence of the (111) and (001) texture components when isotropic and anisotropic grain boundary properties are assumed, e.g. Fig. 12. The notable difference is found when a stored energy difference is present between the two texture components, cf. Fig. 14b. In this case the (111) component is rapidly consumed by the expanding (001) grains. The effect of increasing the difference in stored energy level between the (001) and (111) texture components is shown for comparative purpose by the blue and red lines in Fig. 14b. The black lines represent 20 % less stored energy in the (001) grains compared to the (111) grains while the blue and red lines represent 50 % and 90 % less stored energy in the (001) grains, respectively. It is evident that the general trend of rapid consumption of the (001) texture component by the (111) component is maintained in these cases, the difference being at what point in time the (001) component starts to dominate over the (111)

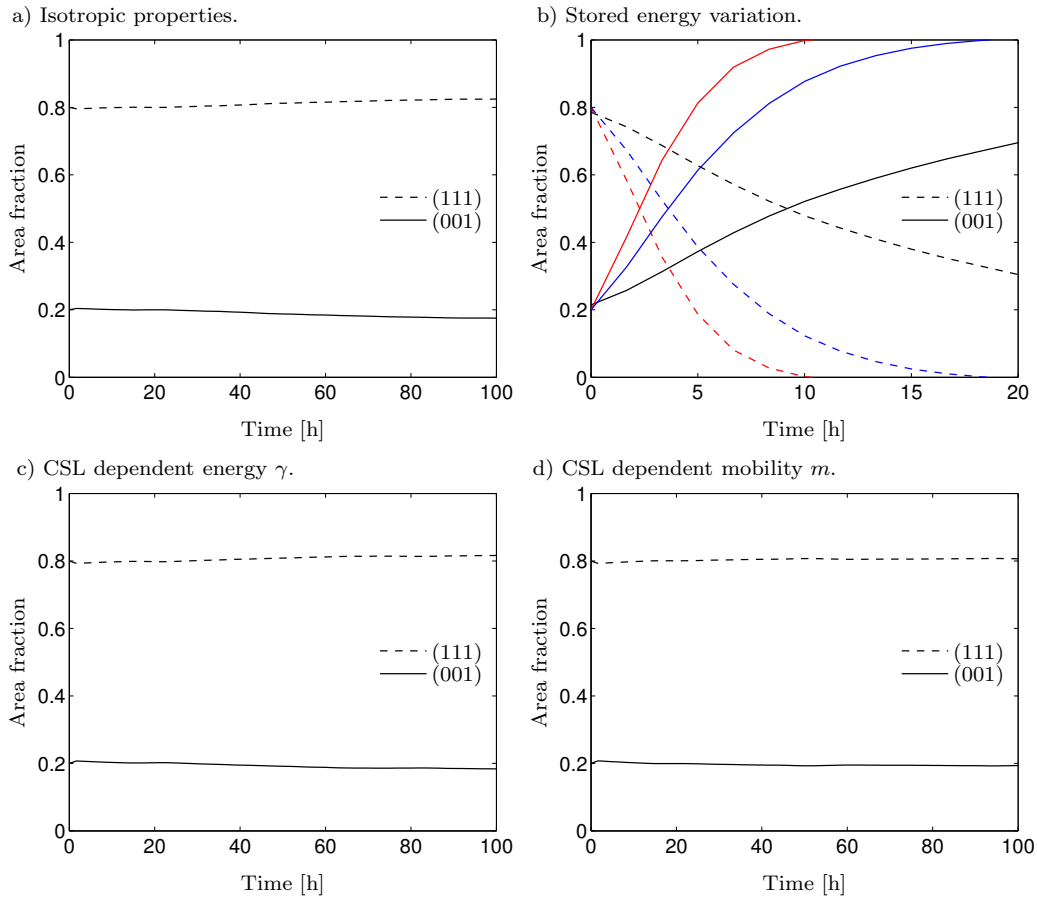

Figure 14: Evolution of the area fractions of the (111) and (001) texture components in the different simulations: a) isotropic properties, b) stored energy variations, b) anisotropic grain boundary energy and c) anisotropic grain boundary mobility. In b), graphs in blue and red color show the influence of lowering the stored energy in the (001) texture component relative to that in the (111) components. The black lines represent a 20 % lowering while the blue and red lines represent a 50 % and a 90 % lowering, respectively.

component. The variation seen in Fig. 14b is in close agreement with the results found in the simulations of grain structure evolution during annealing of Cu thin films in [2], where assumptions on grain growth driving forces were employed that resembles the present stored energy variation. As noted in relation to Fig. 12d, this is a most likely mechanism behind abnormal grain growth in relation to self-annealing in Cu thin films. The growth of the (001) component at the expense of the (111) fiber is also observed in the experiments on microstructure evolution in thin Cu films performed in [18].

Apart from in Fig. 14b, the graphs in Fig. 14 represent an almost constant presence of the two texture components throughout the annealing process. But taking a closer look at the variations of the two texture components in the cases where stored energy is not considered, the trends seen in Fig. 15 become visible. The area fractions of (111) and (001)

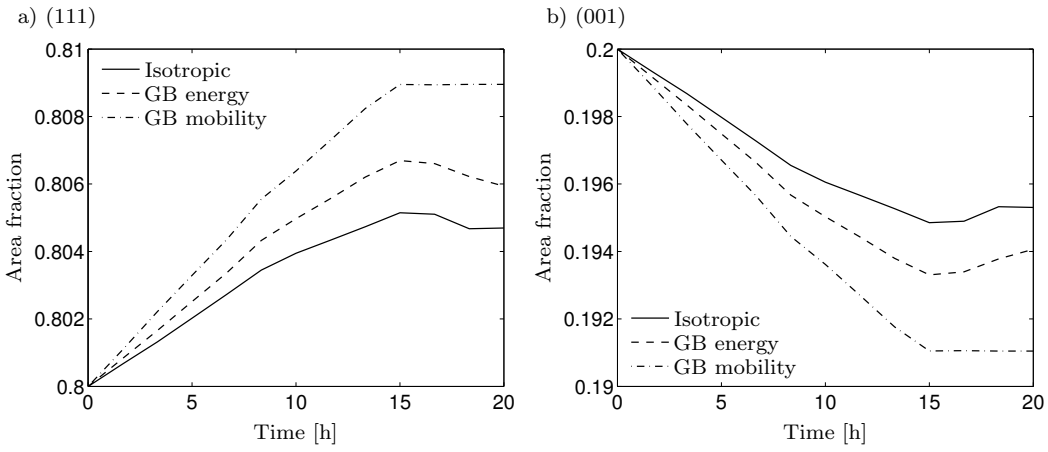

Figure 15: Evolution of the area fractions of texture components of: a) type (111) and b) (001). This is a closer view of the results in Fig. 14, showing the evolution in the absence of stored energy contributions.

textured grains are shown in Fig. 15a and b, respectively. It can be noted that when isotropic or anisotropic grain boundary properties are considered - in the absence of stored energy influence - the content of (111) grains increases while the presence of the (001) component decreases. Although the variations in Fig. 15 are small, only a few percent, the trend is clearly the opposite to what is encountered when stored energy is considered, cf. Fig. 14b. Without sufficient stored energy gradients, the effects of anisotropic grain boundary properties will dominate and the presence of the (001) component will be reduced rather than increased. With the assumptions made in the present modeling approach (relative fractions of texture components, stored energy magnitudes and CSL dependence of γ and m), the stability of the (111) and (001) fiber textures depends on a competition between, rather than on a collaborative effect of, anisotropic grain boundary properties and stored energy variations. This is one probable cause of the sometimes conflicting observations and scattered measurements that can be found in experimental studies on microstructure evolution during self annealing in thin Cu films.

8 Concluding remarks

In the present study, a mesoscale level set model is employed to investigate microstructure evolution during room temperature self-annealing in thin Cu films. The relative impact of anisotropic grain boundary energy and mobility as well as from heterogeneously distributed stored energy is considered. A particular focus lies on the stability of the (111) texture component, that dominates the microstructure in the as-deposited state, in relation to the (001) component that is frequently observed to be promoted during annealing. It is found that the self-annealing process increases the content of a number of low-Σ grain boundaries. This trend is emphasized when taking anisotropic grain boundary properties as well as stored

energy variations into account. The present study further shows that when the (111) texture component has a higher stored energy than the (001) component, the (111) grains are rapidly consumed by growing (001) grains. At the end of the annealing period only the (001) component remains, in line with observations in previous studies found in the literature. In contrast, however, the current investigation also indicates that anisotropic grain boundary properties works in the reverse direction to strengthen the presence of the (111) component over the (001) fiber. These competing mechanisms are likely to be one reason for the considerable diversity in experimental observations of the microstructure evolution during this kind of annealing processes.

Another characteristic feature during self-annealing in thin Cu films is abnormal grain growth, which has been observed in a number of experimental studies. In the present work it is found that anisotropic grain boundary properties, in terms of grain boundary energy or mobility, does not suffice to promote any abnormal growth behavior. In contrast, when considering stored energy variations, (001)-textured grains grow much faster than grains belonging to the (111) component. This promotes abnormal growth of the (001) grains, which is observable in the simulations up until the point where all (111) grains are consumed, leaving a purely (001) textured material after a certain annealing period. The duration of this period depends on the relative levels of stored energy in the two competing texture components.

As an outlook towards future work, it can be noted that the current 2D model poses some restrictions on the microstructure features that can be considered. Although a quasi-columnar grain structure is a reasonable assumption for thin Cu films, a 3D study would allow, for example, consideration of how the inclination of the grain boundary planes influence the anisotropy of properties such as grain boundary energy and mobility. Further, some experimental studies indicate that the thickness of the film has an impact on the microstructure evolution. A free-standing copper film is considered in the present case to avoid the additional influence of interactions with a substrate. This is done in order to isolate the different mechanisms that are investigated and keep the investigation as clear as possible. This means that the influence of the top and bottom film surfaces is not considered. As a consequence of this, thermal grooving is not captured, whereby no stagnation mechanism is present in the model to eventually halt the microstructure evolution. It can be noted that the influence of the top and bottom surfaces can be approximated as done, for example, in [2] where a stagnation criterion is introduced and where an out-of-plane grain boundary curvature is estimated from the film thickness. However, the surface energy driving force for grain boundary migration can be expected to be about two orders of magnitude lower than that due to grain boundary energy, and five orders of magnitude lower than that due to stored energy differences, cf. [41]. In addition, several aspects of the annealing process are strongly temperature dependent, and the variation of annealing behavior with temperature is naturally of additional interest. Regarding these aspects, it can be noted that the present level set-based modeling approach does not pose any restrictions towards performing such studies, which will serve as topics for forthcoming work.

Acknowledgment

H. Hallberg gratefully acknowledges funding from the Swedish Research Council (Vetenskapsrådet, VR) under grant 2012-4231. The *ab initio* modeling in this work was performed using computational resources provided by the Swedish National Infrastructure for Computing (SNIC) at the National Supercomputer Centre (NSC), Linköping University, and at the High Performance Computing Center North (HPC2N), Umeå University.

References

[1] J.W. Patten, E.D. McClanahan, and J.W. Johnston. Room-temperature recrystallization in thick bias-sputtered copper deposits. *J. Appl. Phys.*, 42(11):4371–4377, 1971.

[2] R. Carel, C.V. Thompson, and H.J. Frost. Computer simulation of strain energy effects VS surface and interface energy effects on grain growth in thin films. *Acta Mater.*, 44:2419–2494, 1996.

[3] C. Lingk and M.E. Gross. Recrystallization kinetics of electroplated Cu in damascene trenches at room temperature. *J. Appl. Phys.*, 84(10):5547–5553, 1995.

[4] J.M.E. Harper, C. Cabral Jr., P.C. Andriacacos, L. Gignac, I.C. Noyan, K.P. Rodbell, and C.K. Hu. Mechanisms for microstructure evolution in electroplated copper thin films near room temperature. *J. Appl. Phys.*, 86(5):2516–2525, 1999.

[5] W.H. Teh, L.T. Koh, S.M. Chen, J. Xie, C.Y. Li, and P.D. Foo. Study of microstructure and resistivity evolution for electroplated copper films at near-room temperature. *Microelectron. J.*, 32:579–585, 2001.

[6] C.V. Thompson and R. Carel. Texture development in polycrystalline thin films. *Mater. Sci. Eng. B*, 32:211–219, 1995.

[7] C.V. Thompson and R. Carel. Stress and grain growth thin films. *J. Mech. Phys. Solids*, 44(5):657–673, 1996.

[8] S. Lagrange, S.H. Brongersma, M. Judelewicz, A. Saerens, I. Vervoort, E. Richard, R. Palmans, and K. Maex. Self-annealing characterization of electroplated copper films. *Microelectron. Eng.*, 50:449–457, 2000.

[9] C. Lingk, M.E. Gross, and W.L. Brown. Texture development of blanket electroplated copper films. *J. Appl. Phys.*, 87(5):2232–2236, 2000.

[10] C.-Y. Yang, J.S. Jeng, and J.S. Chen. Grain growth, agglomeration and interfacial reaction of copper interconnects. *Thin Solid Films*, 420-421:398–402, 2002.

[11] J.G. Brons and G.B. Thompson. A comparison of grain boundary evolution during grain growth in fcc metals. *Acta Mater.*, 61:3936–3944, 2013.

[12] L.M. Gignac, K.P. Rodbell, C. Cabral Jr., P.C. Andricacos, P.M. Rice, R.B. Beyers, P.S. Locke, and S.J. Klepeis. Characterization of plated Cu thin film microstructures. *Mat. Res. Soc. Symp. Proc.*, 564:373–378, 1999.

[13] S.H. Brongersma, E. Kerr, I. Vervoort, A. Saerens, and K. Maex. Grain growth, stress and impurities in electroplated copper. *J. Mater. Res.*, 17(3):582–589, 2002.

[14] J.A. Thornton and D.W. Hoffman. Stress-related effects in thin films. *Thin Solid Films*, 171:5–31, 1989.

[15] W. Wu, D. Ernur, S.H. Brongersma, M. Van Hove, and K. Maex. Grain growth in copper interconnect lines. *Microelectron. Eng.*, 76:190–194, 2004.

[16] V. Carreau, S. Maitrejean, Y. Brechet, M. Verdier, D. Bouchu, and G. Passemard. Cu grain growth in interconnect trenches – Experimental characterization of the overburden effect. *Microelectron. Eng.*, 85:2133–2136, 2008.

[17] H.J. Frost. Microstructural evolution in thin films. *Mater. Charact.*, 32:257–273, 1994.

[18] K. Pantleon and M.A.J. Somers. *In situ* invsetigation of the microstructure evolution in nanocrystalline copper electrodeposits at room temperature. *J. Appl. Phys.*, 100:114319, 2006.

[19] C. Detavernier, S. Rossnagel, C. Noyan, S. Guha, C. Cabral Jr., and C. Lavoie. Thermodynamics

and kinetics of room-temperature microstructural evolution in copper films. *J. Appl. Phys.*, 94(5):2874–2881, 2003.
[20] M. Stangl, M. Lipták, A. Fletcher, J. Acker, J. Thomas, H. Wendrock, S. Oswald, and K. Wetsig. Influence of initial microstructure and impurities on Cu room-temperature recrystallization (self-annealing). *Microelectron. Eng.*, 85:534–541, 2008.
[21] K. Kinosita. Recent developments in the study of mechanical properties of thin films. *Thin Solid Films*, 12:17–28, 1972.
[22] W.F. Schottky and M.B. Bever. On the excess energy of electrolytically deposited silver. *Acta Metall.*, 7:199–202, 1959.
[23] W.D. Nix. Mechanical properties of thin films. *Metal. Trans. A*, 20A:2217–2245, 1979.
[24] M.-S. Yoon, Y.-J. Park, and Y.-C. Joo. Impurity redistribution in electroplated Cu films during self-annealing. *Thin Solid Films*, 408:230–235, 2002.
[25] M. Stangl, J. Acker, V. Dittel, W. Gruner, V. Hoffman, and K. Wetzig. Characterization of electroplated copper self-annealing with investigations focused on incorporated impurities. *Microelectron. Eng.*, 82:189–195, 2005.
[26] P. Sonnweber-Ribic, P.A. Gruber, G. Dehm, H.P. Strunk, and E. Arzt. Kinetics and driving forces of abnormal grain growth in thin cu films. *Acta Mater.*, 60:2397–2406, 2012.
[27] H. Lee, S.S. Wong, and S.D. Lopatin. Correlation of stress and texture evolution during self- and thermal annealing of electroplated Cu films. *J. Appl. Phys.*, 93(7):3796–3804, 2003.
[28] K. Ueno, T. Ritzdorf, and S. Grace. Seed layer dependence of room-temperature recrystallization in electroplated copper films. *J. Appl. Phys.*, 86(9):4930–4935, 1999.
[29] C.E. Murray, K.P. Rodbell, and P.M. Vereecken. Underlayer effects on texture evolution in copper films. *Thin Solid Films*, 503:207–211, 2006.
[30] G. Brunoldi, S. Guerrieri, S.G. Alberici, E. Ravizza, G. Tallarida, C. Wiemer, and T. Marangon. Self-annealing and aging effect characterization on copper seed thin films. *Microelectron. Eng.*, 82:289–295, 2005.
[31] W.Q. Zhang, A.D. Li, G.B. Ma, K.B. Yin, Y.D. Xia, Z.G. Liu, C.Y. Chan, K.L. Cheung, M.W. Bayes, and K.W. Yee. Interpretation of texture changes during self-annealing of electroplated copper. *Microelectron. Eng.*, 87:2488–2494, 2010.
[32] W.W. Mullins. The effect of thermal grooving on grain boundary motion. *Acta Metall.*, 6:414–427, 1958.
[33] E.A. Holm and S.M. Foiles. How grain growth stops: A mechanism for grain-growth stagnation in pure metals. *Science*, 328:1138–1141, 2010.
[34] H. Hallberg, B. Svendsen, T. Kayser, and M. Ristinmaa. Microstructure evolution during dynamic discontinuous recrystallization in particle-containing Cu. *Comput. Mater. Sci.*, 84:327–338, 2014.
[35] D.G. Brandon. The structure of high-angle grain boundaries. *Acta Metall.*, 14(11):1479–1484, 1966.
[36] J.K. Mackenzie. Second paper on statistics associated with the random disorientation of cubes. *Biometrika*, 45(1-2):229–240, 1958.
[37] H. Grimmer. Disorientations and coincidence rotations for cubic lattices. *Acta Cryst.*, A30:685–688, 1974.
[38] A.P. Sutton and R.W. Balluffi. *Interfaces in Crystalline Materials*. Oxford University Press, Oxford, UK, second edition, 2007.
[39] G.N. Hassold, E.A. Holm, and M.A. Miodownik. Accumulation of coincidence site lattice boundaries during grain growth. *Mater. Sci. Technol.*, 19:683–687, 2003.
[40] K.G.F. Janssens, D. Raabe, E. Kozeschnik, M.A. Miodownik, and B. Nestler. *Computational Materials Engineering*. Elsevier Academic Press, London, UK, 2007.
[41] G. Gottstein and L.S. Shvindlerman. *Grain Boundary Migration in Metals*. CRC Press, Boca Raton, Florida, USA, 2010.
[42] F.J. Humphreys. A unified theory of recovery, recrystallization and grain growth, based on stability and growth of cellular microstructures - I. The basic model. *Acta Mater.*, 45(10):4231–4240, 1997.
[43] F.J. Humphreys and M. Hatherly. *Recrystallization and related annealing phenomena*. Pergamon,

New York, second edition, 2004.
[44] P.R. Rios, F. Siciliano Jr., H.R.Z. Sandim, R.L. Plaut, and A.F. Padilha. Nucleation and growth during recrystallization. *Mater. Res.*, 8(3):225–238, 2005.
[45] K.G.F. Janssens, D. Olmsted, E.A. Holm, S.M. Foiles, S.J. Plimpton, and P.M. Derlet. Computing the mobility of grain boundaries. *Nat. Mater.*, 5:124–127, 2006.
[46] B. Schönfelder, G. Gottstein, and L.S. Schvindlerman. Atomistic simulations of grain boundary migration in copper. *Metall. Mater. Trans. A*, 37A:1757–1771, 2006.
[47] D.C. Hinz and J.A. Szpunar. Modeling the effect of coincidence site lattice boundaries on grain growth textures. *Phys. Rev. B*, 52(14):9900–9909, 1995.
[48] E.A. Holm, G.N. Hassold, and M.A. Miodownik. On misorientation distribution evolution during anisotropic grain growth. *Acta Mater.*, 49:2981–2991, 2001.
[49] A. Kazaryan, Y. Wang, S.A. Dregia, and B.R. Patton. Grain growth in systems with anisotropic boundary mobility: Analytical model and computer simulation. *Phys. Rev. B*, 63:184102, 2001.
[50] A. Kazaryan, Y. Wang, S.A. Dregia, and B.R. Patton. Grain growth in anisotropic systems: comparison of effects of energy and mobility. *Acta Mater.*, 50:2491–2502, 2002.
[51] A. Kazaryan, Y. Wang, S.A. Dregia, and B.R. Patton. On the theory of grain growth in systems with anisotropic boundary mobility. *Acta Mater.*, 50:499–510, 2002.
[52] H. Ogawa. Gbstudio: A builder software on periodic models of CSL boundaries for molecular simulation. *Mater. Trans.*, 47(11):2706–2710, 2006.
[53] G. Kresse and J. Hafner. *Ab initio* molecular dynamics for liquid metals. *Phys. Rev. B*, 47(1):558–561, 1993.
[54] G. Kresse and J. Hafner. *Ab initio* molecular-dynamics simulation of the liquid-metal–amorphous-semiconductor transition in germanium. *Phys. Rev. B*, 49(20):14251–14269, 1994.
[55] G. Kresse and J. Furthmüller. Efficient iterative schemes for *ab initio* total-energy calculations using a plane-wave basis set. *Phys. Rev. B*, 54(16):11169–11186, 1996.
[56] G. Kresse and J. Furthmüller. Efficiency of ab-initio total energy calculations for metals and semiconductors using a plane-wave basis set. *Comput. Mater. Sci.*, 6(1):15–50, 1996.
[57] P.E. Blöchl. Projector augmented-wave method. *Phys. Rev. B*, 50(24):17953–17979, 1994.
[58] G. Kresse and D. Joubert. From ultrasoft pseudopotentials to the projector augmented-wave method. *Phys. Rev. B*, 59(3):1758–1775, 1999.
[59] J.P Perdew, K. Burke, and M. Ernzerhof. Generalized gradient approximation made simple. *Phys. Rev. Lett.*, 77(18):3865–3868, 1996.
[60] J.P. Perdew, K. Burke, and M. Ernzerhof. Generalized gradient approximation made simple [Phys. Rev. Lett. 77, 3865 (1996)]. *Phys. Rev. Lett.*, 78(7):1396–1396, 1997.
[61] P. Pulay. Convergence acceleration of iterative sequences. The case of SCF iteration. *Chem. Phys. Lett.*, 73(2):393–398, 1980.
[62] H.J. Monkhorst and J.D. Pack. Special points for Brillouin-zone integrations. *Phys. Rev. B*, 13(12):5188–5192, 1976.
[63] M. Methfessel and A.T. Paxton. High-precision sampling for Brillouin-zone integration in metals. *Phys. Rev. B*, 40(6):3616–3621, 1989.
[64] L. Wan and S. Wang. Shear response of the $\sigma 9\langle 110\rangle\{221\}$ symmetric tilt grain boundary in fcc metals studied by atomistic simulation methods. *Phys. Rev. B*, 82(21):214112, 2010.
[65] V.V. Bulatov, B.W. Reed, and M. Kumar. Grain boundary energy function for fcc metals. *Acta Mater.*, 65:161–175, 2014.
[66] D.E. Spearot. *Atomistic Calculations of Nanoscale Interface Behavior in FCC Metals*. PhD thesis, Georgia Institute of Technology, 2005.
[67] L.E. Murr. *Interfacial Phenomena in Metals and Alloys*. Addison-Wesley Educational Publishers Inc., Reading, Massachusetts, USA, 1975.
[68] S. Osher and J.A. Sethian. Fronts propagating with curvature dependent speed: Algorithms based on Hamilton-Jacobi formulations. *J. Comput. Phys.*, 79:12–49, 1988.
[69] H. Hallberg. A modified level set approach to 2D modeling of dynamic recrystallization. *Modell. Simul. Mater. Sci. Eng.*, 21(8):085012, 2013.
[70] M. Bernacki, H. Resk, T. Coupez, and R.E. Logé. Finite element model of primary recrystalliza-

tion in polycrystalline aggregates using a level set framework. *Modell. Simul. Mater. Sci. Eng.*, 17:1–22, 2009.
[71] M. Elsey, S. Esedoglu, and P. Smereka. Simulations of anisotropic grain growth: Efficient algorithms and misorientation distributions. *Acta Mater.*, 61:2033–2043, 2013.
[72] H. Hallberg. Influence of anisotropic grain boundary properties on the evolution of grain boundary character distribution during grain growth – a 2D level set study. *Modell. Simul. Mater. Sci. Eng.*, 22(8):085005, 2014.
[73] H.S. Kim, Y. Estrin, E.Y. Gutmanas, and C.K. Rhee. A constitutive model for densification of metal compacts: the case of copper. *Mater. Sci. Eng.*, 307:67–73, 2001.
[74] H.J. Frost and M.F. Ashby. *Deformation-Mechanism Maps*. Pergamon Press, 1982.
[75] T. Surholt and C. Herzig. Grain boundary self-diffusion in Cu polycrystals of different purity. *Acta Mater.*, 45(9):3817–3823, 1997.
[76] M. Hillert. On the theory of normal and abnormal grain growth. *Acta Metall.*, 13:227–238, 1965.
[77] P.R. Rios. Abnormal grain growth development from uniform grain size distributions. *Acta Mater.*, 45(4):1785–1789, 1997.
[78] A.D. Rollett. Overview of modeling and simulation of recrystallization. *Prog. Mater. Sci.*, 42:79–99, 1997.
[79] P. Pant, K.W. Schwarz, and S.P. Baker. Dislocation interactions in thin FCC metal films. *Acta Mater.*, 51:3243–3258, 2003.
[80] R.S. Fertig III and S.P. Baker. Dislocation dynamics simulations of dislocation interactions and stresses in thin films. *Acta Mater.*, 58(15):5206–5218, 2010.
[81] M. Hommel and O. Kraft. Deformation behavior of thin copper films on deformable substrates. *Acta Mater.*, 49:3935–3947, 2001.
[82] S.P. Baker, A. Kretschmann, and E. Arzt. Thermomechanical behavior of different texture components in Cu thin films. *Acta Mater.*, 49(12):2145–2160, 2001.
[83] H. Ljungcrantz, M. Odén, L. Hultman, J.E. Greene, and J.-E. Sundgren. Nanoindentation studies of single-crystal (001)-, (011)-, and (111)-oriented TiN layers on MgO. *J. Appl. Phys.*, 80(12):6725–6733, 1996.
[84] M. Ohring. *Materials science of thin films*. Academic Press, San Diego, California, USA, 2001.
[85] R. Abermann and R. Koch. The internal stress in thin silver, copper and gold films. *Thin Solid Films*, 129(1):71–78, 1985.
[86] B. Schönfelder, G. Gottstein, and L.S. Schvindlerman. Comparative study of grain-boundary migration and grain-boundary self-diffusion of [100] twist-grain boundaries in copper by atomistic simulations. *Acta Mater.*, 53:1597–1609, 2005.
[87] Y. Pan and B.L. Adams. On the CSL grain boundary distributions in polycrystals. *Scr. Metall. Mater.*, 30(8):1055–1060, 1994.